Modeling and Analysis of High-Q Resonant-Fin Transistors

Ehrentraud Hager, *Student Member, IEEE*, Richard Hudeczek, Peter Baumgartner, *Member, IEEE*, and Harald Pretl, *Senior Member, IEEE*

***Abstract*—This article presents a method for modeling high-*Q* resonant-fin transistors with focus on circuit design simulations. The model is implemented for simulations in a SPICE-like design environment and is based on two basic properties of the resonator device: the mechanical spectral behavior and the electro-mechanical-transfer function. The spectral model operates in the mechanical pressure regime, while the mobility model converts this pressure into a mobility change inside the channel of the transistor and is hence, generating an ac current at the output of the device. The model also includes the electrical transistor characteristic for the input and the output of the resonator. This enables accurate and fast circuit simulations with a standard SPICE simulator, e.g., for the design of frequency synthesizer circuits. The model is validated against finite element method (FEM) simulations at an artificially damped quality factor of $Q = 500$. Also, simulation results for a quality factor of $Q = 50\,000$ are shown, to prove the full functionality of the electrical model.**

***Index Terms*—Circuit simulation, electrical model, FinFET, finite element analysis, high *Q*-factor, modified Butterworth–Van Dyke (MBVD), resonant–fin transistor (RFT), resonator.**

I. Introduction

THE introduction of advanced communication standards such as long term evolution (LTE) and 5G New Radio drives the development of smaller and more compact devices.

Manuscript received June 2, 2021; revised July 7, 2021; accepted July 8, 2021. Date of publication July 26, 2021; date of current version August 23, 2021. This work was supported in part by the Austrian Federal Ministry for Digital and Economic Affairs, in part by the National Foundation for Research, Technology and Development, and in part by the Christian Doppler Research Association. The review of this article was arranged by Editor K. Xia. *(Ehrentraud Hager and Richard Hudeczek contributed equally to this work.) (Corresponding author: Ehrentraud Hager.)*

Ehrentraud Hager is with the Christian Doppler Laboratory for Digitally Assisted RF Transceivers for Future Mobile Communications, Johannes Kepler University, 4040 Linz, Austria, and also with the Institute for Integrated Circuits, Johannes Kepler University, 4040 Linz, Austria (e-mail: ehrentraud.hager@jku.at).

Richard Hudeczek is with the Department of Electrical Engineering and Information Technology, Technical University of Munich, 80333 Munich, Germany, and also with Intel Germany, 85579 Neubiberg, Germany (e-mail: richard.hudeczek@intel.com).

Peter Baumgartner is with Intel Germany, 85579 Neubiberg, Germany.

Harald Pretl is with the Institute for Integrated Circuits, Johannes Kepler University, 4040 Linz, Austria.

Color versions of one or more figures in this article are available at https://doi.org/10.1109/TED.2021.3097302.

Digital Object Identifier 10.1109/TED.2021.3097302

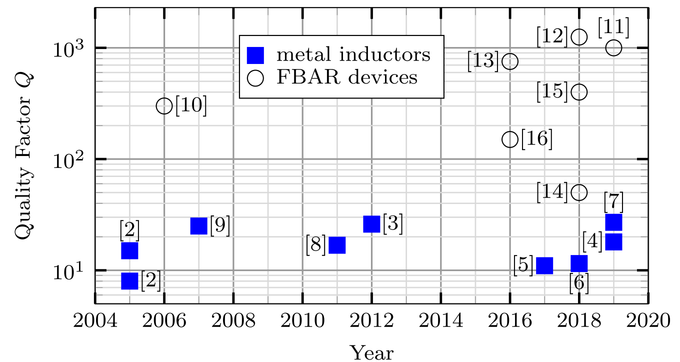

Fig. 1. Comparison of different resonator implementations and their achieved quality factor *Q*.

Additionally maintaining and improving power consumption at increasing frequencies is a critical problem statement for radio frequency (RF) circuit design. Despite good scaling of active devices with every process node, passive components like on-chip metal inductors see hardly any improvement [1], [2]. However, inductors and resonators are key components for frequency generation and analog filter design in RF circuit designs. To generate high-performance filters and clock signals of high spectral purity, a high-quality factor (Q-factor) of the used resonator is needed. The most common implementation of a resonant circuit for mobile communication transceiver designs is the well-known LC-tank. It can be integrated very easily to on-chip in standard CMOS processes and is a widely used technique to realize oscillator tanks and analog filters. However, this implementation type suffers from low Q-factors of the metal coil, when comparing it to an off-chip crystal quartz resonator. Another drawback is the area consumption of an LC-tank, as it does not scale with the process node. The highest Q-factors can be achieved using microelectro mechanical systems (MEMSs) like film bulk acoustic wave resonators (FBARs).

Fig. 1 shows a comparison of a selection of different resonator implementations, demonstrated in [2]–[16], and the achieved Q-factor over the years. While traditional metal inductors achieve maximum values of approximately 30, FBARs show much higher ratings in the range of 1000 and beyond. Their biggest disadvantage is the difficult integration to CMOS technologies. Current approaches are using multichip-modules or attempts of monolithic integration including 1) the "MEMS-last" approach with

This work is licensed under a Creative Commons Attribution 4.0 License. For more information, see https://creativecommons.org/licenses/by/4.0/

material-deposition on fully processed CMOS chips and 2) the "MEMS-in-the-middle" approach, where the resonators are formed by postprocessing the metal stack. Both methods require additional processing steps, which raise production costs and complexity of the overall system [17].

Recent research activities like [18] have shown a possibility to implement MEMS resonators fully embedded in standard CMOS FinFET processes with promising results in frequency and Q-factor. The presented resonant fin transistor (RFT) utilizes the geometric properties of a standard CMOS FinFET process to drive and sense acoustic vibrations in the solid CMOS front-end-of-line (FEOL) in an electric fashion without the need for additional postprocessing or special packaging. This novel type of resonator is potentially capable of generating high-frequency signals in the range of tens of gigahertz with an exceptional spectral purity, with Q-factors over 40 000, enabling new possibilities for frequency generation for modern mobile communication transceiver designs.

To make use of this device in circuit design simulations, accurate models have to be generated. Therefore, in this work, a novel electrical device-model for the RFT is proposed, to allow the usage and scaling of the resonator in RF circuit design by modeling electrical and electro-mechanical effects of the device for circuit simulators. In Section II, the electro-mechanical simulation of a resonator unit cell using a multiphysics simulator and its analysis is shown. Section III discusses the mapping of the electro-mechanical behavior to a fully electrical model, enabling the usage in circuit simulators. The full device model is presented in Section IV, including a validation of the model against the electro-mechanical simulations results.

II. MECHANICAL SIMULATIONS

To gain a deeper understanding of the electro-mechanical behavior of the RFT, 3-D finite element method (FEM) simulations were carried out with a commercially available simulator.[1] From these results, the parameters for a later circuit level modeling are retrieved.

A. FinFET MEMS Working Principle

The working principle of the RFT is based on MOS capacitor actuation, which couples to a mechanical eigenmode inside a FinFET gate with hundreds of adjacent fins [18]. The mechanical eigenmode inside the common gate is sensed at a differentially wired transistor pair. The deformation of the FinFET channel, caused by the mechanical eigenmode, leads to a modulation of the electron mobility and therefore the transistor current. The resonant frequency is strongly influenced by the material properties and spatial dimensions of the device. Moreover, for best functionality, i.e., the largest current modulation at the output, the pressure in the channel needs to be as large as possible. To reach the large Q-factor reported in [18], an acoustic Bragg mirror is required in the back-end-of-line (BEOL). Mechanical losses of the cavity can be reduced if the resonant frequency lies within any acoustic bandgap of the BEOL mirror [19], [20].

[1]COMSOL Multiphysics v. 5.5. www.comsol.com

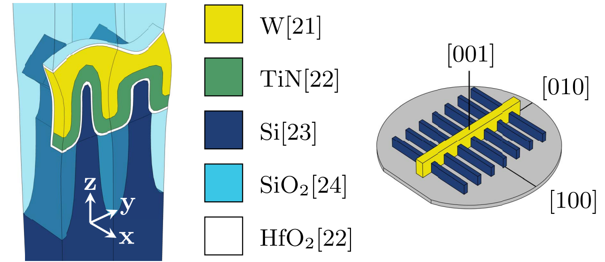

Fig. 2. Unit cell for the mechanical 3-D-FEM simulations with the used materials and orientation of the RFT on the assumed wafer. The deformation of the unit cell illustrates the eigenmode and is not to scale.

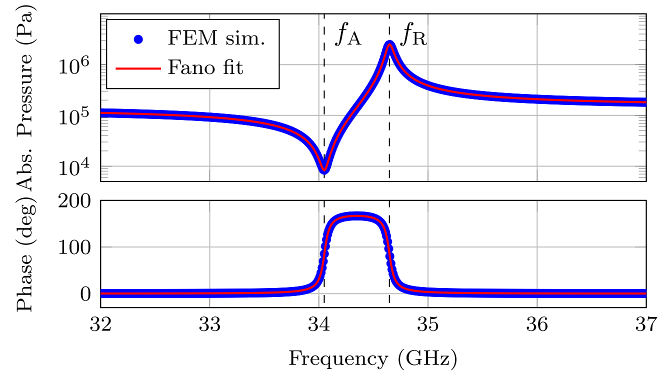

Fig. 3. Response of mode 2 under ac excitation and complex valued Fano fit to the absolute pressure and phase.

The simulation volume was reduced to the smallest periodic unit cell, covering only two adjacent fins, depicted in Fig. 2. This is required to describe the mechanical and electrical differential nature of the eigenmode in the assumption of an infinite cavity. Only half of the gate is modeled with symmetric boundary conditions along the fin direction (X). The vertical directions are terminated by perfectly matched layers in the far distance (Z) and Floquet–Bloch boundary conditions are deployed along the gate direction (Y). The FinFET structure was modeled to typical 16 nm dimensions. The BEOL mirror was omitted to increase flexibility of the electrical model, as the BEOL can vary strongly from process to process. The silicon wafer used in the simulation is mechanically anisotropic and (100) oriented [23]. The fins and gate are biased at $V_{\mathrm{drive}} = 40$ mV and $V_{\mathrm{G}} = 800$ mV, respectively. Both fins are driven with a sinusoidal amplitude of $v_{\mathrm{drive}} = 30$ mV and a phase difference of $\phi_{\mathrm{drive}} = 180°$ in-between them [18]. The absolute pressure variation, derived from the integrated Cauchy stress tensor inside one of the FinFET channels, with regard to the actuation frequency is depicted in Fig. 3. The spectrum obtained from the ac simulation exhibits a distinct peak at the frequency of the mechanical eigenmode. In addition to the main resonance (f_{R}) also an antiresonance (f_{A}) can be observed at a lower frequency where the pressure inside the channel drops to almost zero. The simulation was limited to $Q = 500$ via Rayleigh damping for illustrative purposes [25]. Thus, also the maximum pressure for this mode, which scales with the Q-factor, is limited to 7.2 MPa.

1) Quality Factor: To model the RFT MEMS on a circuit level, the quantities f_{R}, f_A, Q_{R}, and Q_{A} have to be retrieved from the spectrum depicted in Fig. 3. The asymmetric shape,

also known as Fano-resonance, allows to retrieve the Q-factor of the main resonance [26]. It can be described by

$$S(f) = a + b\frac{2(f - f_\mathrm{R}) - q f_{\mathrm{R},BW}}{2(f - f_\mathrm{R}) - j f_{\mathrm{R,BW}}} \tag{1}$$

with a and b being complex valued prefactors, f_R the resonant frequency, $f_\mathrm{R,BW}$ the bandwidth of the resonance and q the Fano parameter which describes the overall symmetry of the Fano resonance [27]. The complex valued function is fitted to both amplitude and phase simultaneously allowing the retrieval of the resonant frequency and bandwidth and thus, the consecutive calculation of the Q-factor with $Q_\mathrm{R} = f_\mathrm{R}/f_\mathrm{R,BW}$. It should be noted that due to the artificial Rayleigh damping the Q-factor retrieved from the Fano fit is identical to the prescribed value. The Fano fitting, while giving some insight into the nature of the resonance mechanisms, however, has some drawbacks when it comes to gathering all information required for the circuit level description of the RFT. Albeit the main resonance is properly described it lacks information for the Q-factor of the antiresonance. A different method allows the extraction of the missing Q-factor from the slope of the phase ϕ at any angular frequency of the spectrum depicted in Fig. 3 with

$$Q_\mathrm{R,A} = \frac{\omega_\mathrm{R,A}}{2}\left|\frac{\partial\phi}{\partial\omega}\right|\Bigg|_{\omega=\omega_\mathrm{R,A}} \tag{2}$$

where $f_\mathrm{R} = \omega_\mathrm{R}/2\pi$ and $f_\mathrm{A} = \omega_\mathrm{A}/2\pi$ are the resonance and antiresonance frequencies, respectively, [28]. The location of the resonance and antiresonance is extracted from the largest and smallest pressure in Fig. 3. Both (1) and (2) return the same Q-factor, with (2) also being used for the retrieval of the Q-factor of the antiresonance. The Q-factor of the antiresonance $Q_\mathrm{A} = 476$ is lower than of the resonance $Q_\mathrm{R} = 500$ due to over damping caused by the Rayleigh formulation for all other frequencies [25].

2) Effective Coupling Coefficient: A further important figure of merit is the effective coupling coefficient

$$k_\mathrm{eff}^2 = \frac{\pi^2}{4}\left(\frac{f_\mathrm{A} - f_\mathrm{R}}{f_\mathrm{R}}\right). \tag{3}$$

It describes the conversion efficiency from electrical to mechanical energy, and vice versa [29]. For the ideal unit cell, the effective coupling coefficient is 4.27%. This value is comparable to AlN FBAR devices [10], [14], [29], [30]. However, as a result of the reduced unit cell, this value is strongly overestimated. In this configuration (compare Fig. 2), every fin is connected, which is typically forbidden by the layout design rule constraints, which are imposed by the foundries. Assuming a larger unit cell of 14 fins and a design rule compliant connection scheme, the effective coupling drops to 0.2%, which is more reasonable at such frequencies [18], [30]. Nevertheless, the model is able to describe a wide range of coupling coefficients, which solely depend on the modeled device.

3) Mobility Variation: For the device to reach optimal performance, it is necessary to reach large pressures inside the FinFET channel as it directly influences the change in electron mobility and thereby the current swing at the output. The peak

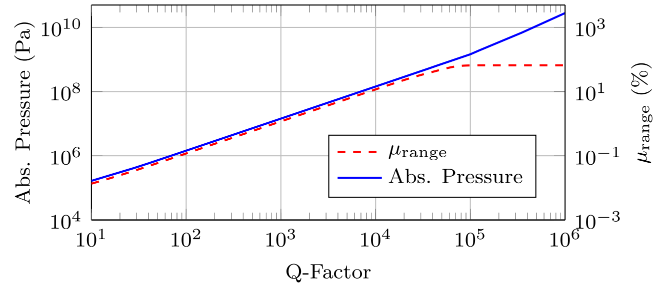

Fig. 4. Dependence of main resonance pressure and mobility change μ_range between fins of opposite phase on the Q-factor.

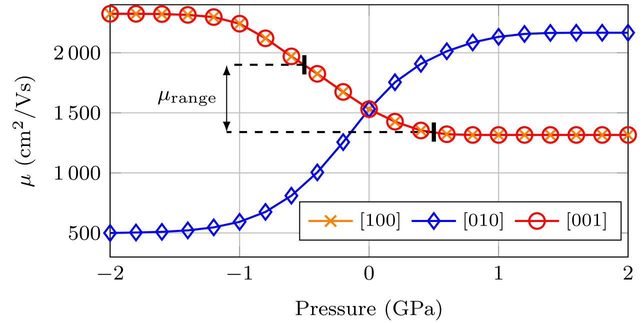

Fig. 5. Electron mobility μ of silicon in dependence on uni-axial stress along [010]. μ_range for a pressure of 0.5 GPa is marked for clarification. Data adapted from [31], [32].

pressure reached at the main resonance f_R in dependence on the Q-factor, while keeping the bias and excitation voltages unchanged, is shown in Fig. 4. It rises nearly linearly for $Q =$ 10–100 000 from 166 kPa to 1.46 GPa. For larger Q-factors, a slight increase is observable; however, these Q-factors are unlikely to be obtained in a real world scenario. The change in electron mobility, however, does not only depend on the mechanical pressure but also the crystallographic orientation of the silicon wafer. For the (100) oriented wafer, the crystal principal axis [100] is parallel to the FinFET channel direction and [010] parallel to the gate, i.e., the cavity, as illustrated in Fig. 2. The mobility variation in (100) silicon for uni-axial stress along [010] is depicted in Fig. 5 [31], [32]. Assuming uni-axial stress along the gate (compare Fig. 2) the mobility change perpendicular to that direction along the FinFET channel, i.e., along [100] has to be considered. At the maximum deflection point for the resonant eigenmode, every other fin has the same absolute pressure, however, with opposite sign, leading to a change in mobility for each fin according to Fig. 5. Interestingly, the mobility change is not symmetric with regard to the sign of the pressure leading to asymmetries in the overall change. The maximal mobility difference at full deflection is

$$\mu_\mathrm{range} = \frac{|\mu_\mathrm{max} - \mu_\mathrm{min}|}{\mu_0} \tag{4}$$

where μ_min and μ_max are the crest and trough mobilities for opposite phases and μ_0 is the unstrained mobility. The range is exemplary shown for a pressure of 0.5 GPa in both fins in Fig. 5. Moreover, the mobility range as well as the required pressure with regard to the Q-factor are shown in Fig. 4.

For small pressures, e.g., at $Q = 500$ with a corresponding fin pressure of 7.2 MPa only an absolute mobility change in the subpercent regime can be achieved. However, with rising pressure attributed to a higher Q-factor, the mobility change rises significantly and saturates for a pressure difference of approximately 2 GPa. Hence, so to maximize the mobility delta in between the two fins a large enough Q-factor is needed. At $Q = 50\,000$, close to the reported value in [18], the absolute mobility range increases to $\mu_{\text{range}} = 50\%$.

III. Electro-Mechanical Model for Circuit Simulation

To use the RFT device in integrated circuits, e.g., oscillators or narrowband filters, the resonator has to be modeled in a fully electrical fashion. This enables the usage of the model in a SPICE-like design environment. The two major aspects of the RFT-device, which should be also reflected in the electrical model, are the spectral mechanical relation of mode actuation and the electro-mechanical relation between pressure and electron mobility described in Section II.

A. Spectral Pressure Model

The spectral electro-mechanical behavior together with the drive mechanism (conversion of voltage into mechanical pressure) is modeled by the spectral pressure model depicted in Fig. 6. Commonly MEMS resonators are modeled with a Modified Butterworth–Van Dyke (MBVD) model [33], [34] completely in the electrical domain by forming parallel and serial resonant circuits representing resonance, antiresonance, and damping effects of the MEMS device. Because of its active four-port nature, the MBVD is not instantly usable as model for the RFT. The spectral model depicted in Fig. 6, however, uses an MBVD inspired impedance model to implement the basic pressure-transfer function of the RFT in an electrical domain useable in a circuit-simulation environment. The spectral pressure characteristic of the RFT is modeled by a series resonant circuit consisting of the inductor L_1 together with the capacitor C_1 and the resistor R_1, and a parallel resonant part formed by again the inductance L_1 and the capacitor C_2 as well as R_2. The resistor R_s enables modeling of additional damping mechanisms. To use this impedance model in a circuit simulator, the correct dc operating point as well as a good decoupling to the output has to be added to the impedance model. In addition, a high-pass (C_{HP} and R_{HP}) with a corner frequency of 10 Hz is added to the model input to enhance the simulator convergence at dc.

The closed-form expression of the impedance formed by the lumped elements L_1, C_1, R_1, C_2, R_2, and R_s can be written as

$$Z(s) = \frac{1}{sC_2} \cdot \frac{1 + sC_1(R_1 + R_s) + s^2 L_1 C_1}{1 + sC_1(R_1 + R_2) + s^2 \frac{L_1 C_1 C_2}{C_2 + C_1}} \tag{5}$$

with the complex frequency $s = j\omega$. The lumped elements can be linked to the quality factors, resonance, and antiresonance frequencies of the resonator [35]. Therefore, (5) can be rewritten to

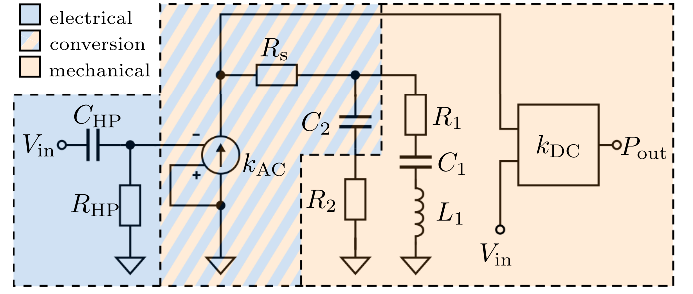

Fig. 6. Schematic of spectral model including impedance model, high-pass, and output-decoupling.

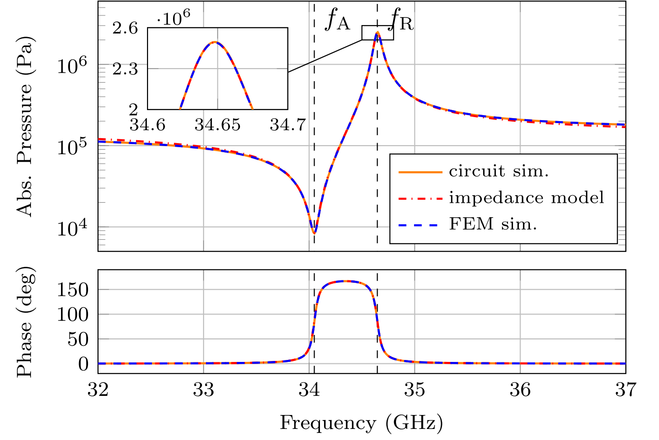

Fig. 7. Simulated output voltage V_{out} of the spectral model and calculated impedance model over frequency in comparison with FEM simulation (see Fig. 3).

$$Z(s) = \frac{1}{sC_2} \cdot \frac{1 + s\frac{1}{\omega_A Q_A} + s^2 \frac{1}{\omega_A^2}}{1 + s\frac{1}{\omega_R Q_R} + s^2 \frac{1}{\omega_R^2}} \tag{6}$$

with Q_A and ω_A the quality factor and frequency of the resonators antiresonance, and Q_R and ω_R being the quality factor and resonance frequency of the main resonance, respectively. For the calculation of component values the quality factors, as well as the resonance and antiresonance frequency have to be either measured or simulated as shown in Section II. The resistor R_s is set to 0 as additional mechanical loss mechanisms on drive side, as well as BEOL effects are not taken into account. The capacitance C_2, representing the static gate-to-fin-capacitance can be simulated by FEM simulation to 38 fF. The remaining capacitance and inductance are calculated to [34]

$$C_1 = C_2 \cdot \left[\left(\frac{\omega_R}{\omega_A} \right)^2 - 1 \right], \quad L_1 = \frac{1}{\omega_A^2 C_1}. \tag{7}$$

The R_1 and R_2 are calculated using the known Q-factors to [29], [34]

$$R_1 = \frac{\omega_A L_1}{Q_A} - R_s, \quad R_2 = \frac{\omega_R L_1}{Q_R} - R_1. \tag{8}$$

In Fig. 7, the frequency response of the spectral model, including decoupling, is shown in comparison to the

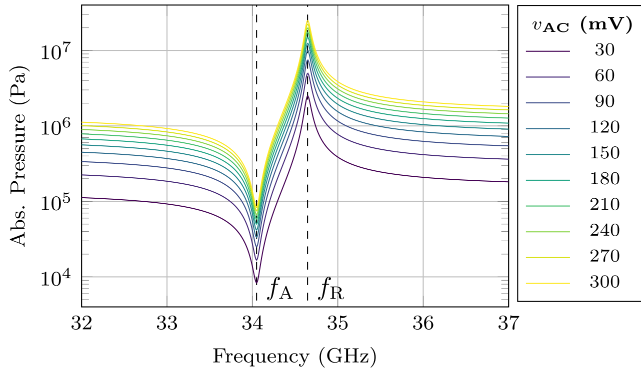

Fig. 8. FEM simulated fin pressure over frequency with dependence on variation of ac drive amplitude v_{ac}.

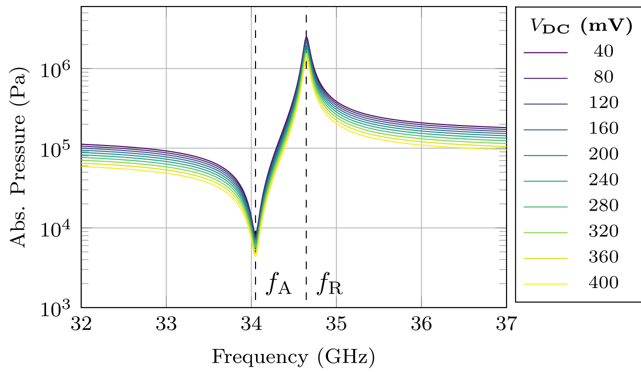

Fig. 9. FEM-simulated fin pressure over frequency with dependence on variation of dc drive level V_{dc}.

impedance calculations from the impedance model and the FEM simulations. The circuit simulation shows a very good fit to the simulation results already presented in Fig. 3. In the range of the resonance frequency, the model closely resembles the FEM simulation with a deviation of 0.12%, while aligning with the impedance model for a greater spectral distance to said resonance.

To model the spectral behavior of the RFT device correctly, two major dependencies have to be taken into account:

1) Dependence on AC Drive Amplitude: Fig. 8 depicts the variation of pressure with actuation frequency and changing ac drive amplitude simulated by the FEM simulation. The pressure increases with increasing ac amplitude. The dc level was kept at a constant 40 mV for this simulation. The slope of the pressure increase per increase interval of the ac amplitude is nearly constant, with a deviation in the range of parts-per-thousand. Hence, for the circuit model, a constant conversion factor $k_{ac} = 33.33$ Pa V^{-1}, which links the ac input voltage to the mechanical pressure in the fin, is chosen. The value for k_{ac} is determined by a fit of the impedance model to simulation results of a base configuration of the resonator ($V_{drive} = 40$ mV and $v_{drive} = 30$ mV) and by weighing the input voltage according to the variation slope. As shown in Fig. 6, the factor k_{ac} is implemented as a voltage-controlled current-source at the input of the model.

2) Dependence on DC Drive Level: The variation due to the dc bias is shown in Fig. 9. The ac amplitude was kept at 30 mV for the simulation, with the pressure decreasing for rising dc bias values. Again, the slope is nearly constant, thus, a fixed factor of $k_{dc} = -1.32$ Pa V^{-1}, as well as a constant offset to match the model to the skew of curves is implemented in a VerilogA block depicted in Fig. 6.

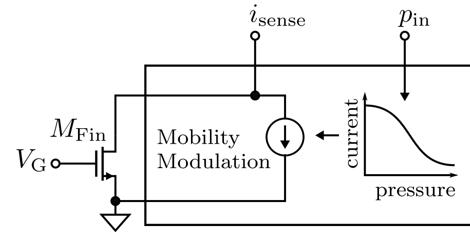

Fig. 10. Schematic of complete mobility model including mobility modulation, modeled in VerilogA, and the sense transistor.

Both factors reflect the variation of the pressure with frequency in dependence on the ac and dc voltages at the drive fin packages for all supported types of simulations, as described in Section IV.

B. Electron Mobility Model

The spectral model described in Section III-A provides at its output a voltage representing the pressure inside a single fin. This voltage level has to be converted into a change in electron mobility in the channel of the sense transistors, to model the complete RFT device behavior. The mobility in [100] direction along the fin, as shown in Fig. 5, is implemented as a VerilogA table model, where the input pressure is mapped to a relative mobility change in the channel. According to the Berkeley short-channel IGFET model-common multigate (BSIM-CMG) FinFET model [36], [37], the drain–source current is indirectly linear dependent on the degradation of the channel mobility. This factor D_{mob} incorporates the vertical mobility degradation due to different scattering mechanisms $D_{mob,0}$ as well as a multiplier parameter U0MULT used for variability modeling with $D_{mob} = D_{mob,0}/\mathrm{U0MULT}$. It can be shown that the following relation holds:

$$I_{DS} \propto \mathrm{U0MULT}. \tag{9}$$

This linear dependence is used to incorporate the mobility change due to the pressure on the fin. As shown in Fig. 10, the mobility change is added as modulated current at the sense node of the model. The dc operating point is set by the transistor M_{Fin}. The input of the pressure/mobility model is electrically shorted to the output, hence, the transistor M_{Fin} is directly connected to the output, defining the output characteristic of the overall RFT-model. Other physical or electrical properties that might be affected by the mobility variation like R_{ON} or V_{TH} are not included in this model.

IV. Complete Device Model

In Fig. 11 the complete RFT circuit model is shown. In addition to the two model parts described in Section III, the input characteristic of the RFT is added. At the gate G and the two drive-inputs D_p and D_n transistors were added to model the capacitive behavior. After the input models,

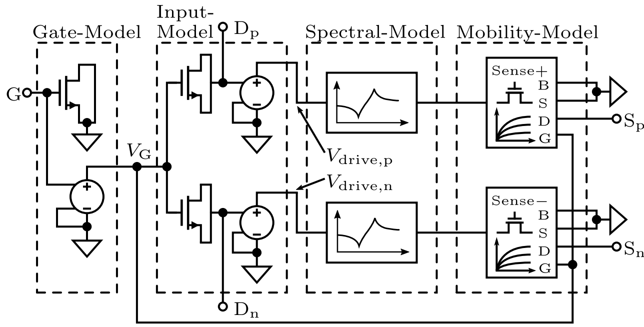

Fig. 11. Block diagram of the electrical RFT model.

follows the spectral model discussed in Section III-A for the differential excitation of the RFT. Each mechanical phase of the RFT is modeled with a separate spectral model, which increases the overall flexibility for different cavity contact configurations. They feed the output models described in Section III-B, which are placed for each of the two sense transistors (sense+ and sense−).

A. Model Comparison to FEM Simulation

The proposed model was verified by circuit simulations for an ideal RFT device, with a single gate, where every other fin is actuated and two sense FinFETs in the center. In Table I, the device configuration used for the comparison of the circuit and FEM simulation are listed. The electrical model is compared to the FEM simulation by the resulting mobility change in the output transistors due to an oscillating input voltage. The mobility variation of the FEM model was obtained by interpolation analogous to the VerilogA model described in Section III-B. Simulations for dc, ac and transient were performed to ensure full functionality of the electrical model. For pure dc simulations, both the FEM and circuit simulation show no mobility variation as is to be expected from the RFT. In Fig. 12 the ac spectrum of the complete RFT device model and FEM simulation are shown. Both simulations are in excellent agreement, with a maximum deviation at the resonance of about 0.5%. The discrepancy originates from a systematic error and minor simplifications when fitting the impedance model, dc and ac variation to the FEM simulation. The absolute mobility value reached of approximately $\Delta\mu = 0.102\%$ for $Q_p = 500$ is solely exemplary and will not yield a functional device. It was chosen to allow for a good comparison between the FEM and circuit simulations. With rising Q-factors FEM simulations, and more explicitly transient FEM simulations, get challenging. With larger Q-factors the pressure rises significantly, as depicted in Fig. 4, and thus for the reported $Q_p = 50\,000$ the circuit simulation yields $\Delta\mu = 50\%$ at the sense FinFETs.

B. High-Q Simulation

To test the model also for large Q-factors as described above, the circuit depicted in Fig. 11 is adapted to a similar configuration as presented in [18]. The sense packets are formed by three adjacent fins, as layout design rules do not allow for single fin contacting. The drive is assumed to

TABLE I
DEVICE CONFIGURATION FOR MODEL VALIDATION

Parameter	Value	Parameter	Value
Q_{res}	499.914	v_{drive}	30 mV
Q_{ares}	492.021	V_{drive}	40 mV
f_{res}	34.646 GHz	V_{sense}	200 mV
f_{ares}	34.049 GHz	V_G	800 mV

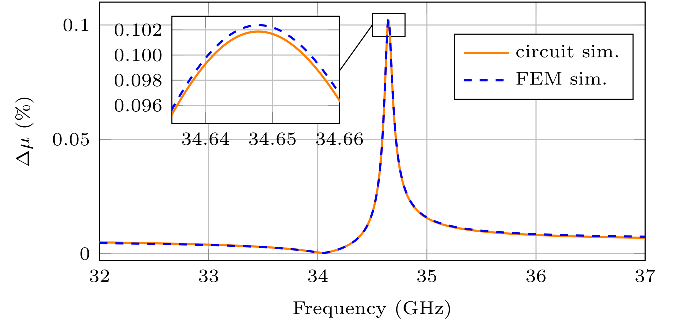

Fig. 12. Frequency-dependent mobility change of the RFT device.

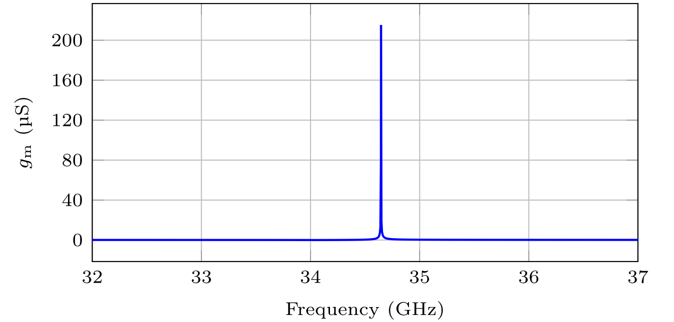

Fig. 13. Transconductance g_m of RFT over frequency.

be ideal. The simulated device reaches a peak mechanical transconductance $g_m = 215.184\ \mu$S as shown in Fig. 13. The transconductance is calculated to

$$g_m = \frac{i_{sense}}{v_{drive}} \tag{10}$$

where v_{drive} is the differential input drive voltage and i_{sense} the differential output current at a load resistor of $R_L = 100\ \Omega$. The observed g_m can be boosted by deploying multiple parallel gates in the cavity, hence, increasing i_{sense} with each additional gate while maintaining the same v_{drive}. In addition, the gap to measurement results shown in [18] might be rooted in different electron mobilities for other wafer orientations, which can strongly influence the transconductance [31], [32], [38].

V. CONCLUSION

In this article, a method for device modeling of high-quality factor RFTs has been presented. This model enables the integration of this novel device type into an electrical SPICE-like simulation framework and therefore allows circuit designs leveraging this resonator. Electrical simulations using the model presented in Section IV show an excellent fit to FEM simulations of the structure presented in [18] and achieve good results and fast simulation time for high-quality factors above 1000. The model can be used in typical simulation scenarios, like dc, ac, harmonic balance, and transient simulations,

enabling circuit analysis close to the resonance frequency of the device. The generic structure of the model leaves room for optimization, incorporating measurement information for drive losses, drive to sense coupling as well as transient startup and expand the scope of application to lower and higher frequencies.

REFERENCES

[1] A. Stillmaker and B. Baas, "Scaling equations for the accurate prediction of CMOS device performance from 180 nm to 7 nm," *Integr., VLSI J.*, vol. 58, pp. 74–81, Jun. 2017, doi: 10.1016/j.vlsi.2017.02.002.

[2] K. Lee *et al.*, "The impact of semiconductor technology scaling on CMOS RF and digital circuits for wireless application," *IEEE Trans. Electron Devices*, vol. 52, no. 7, pp. 1415–1422, Jul. 2005, doi: 10.1109/TED.2005.850632.

[3] G. Li, L. Liu, Y. Tang, and E. Afshari, "A low-phase-noise wide-tuning-range oscillator based on resonant mode switching," *IEEE J. Solid-State Circuits*, vol. 47, no. 6, pp. 1295–1308, Jun. 2012, doi: 10.1109/JSSC.2012.2190185.

[4] A. Bhat and N. Krishnapura, "A 25-to-38 GHz, 195 dB FoMT LC QVCO in 65 nm LP CMOS using a 4-port dual-mode resonator for 5G radios," in *IEEE Int. Solid-State Circuits Conf. (ISSCC) Dig. Tech. Papers*. Piscataway, NJ, USA: Institute of Electrical and Electronics Engineers, Feb. 2019, pp. 412–414, doi: 10.1109/ISSCC.2019.8662502.

[5] C.-C. Li *et al.*, "A 0.2V trifilar-coil DCO with DC-DC converter in 16 nm FinFET CMOS with 188 dB FOM, 1.3 kHz resolution, and frequency pushing of 38 MHz/V for energy harvesting applications," in *IEEE Int. Solid-State Circuits Conf. (ISSCC) Dig. Tech. Papers*, Feb. 2017, pp. 332–333, doi: 10.1109/ISSCC.2017.7870396.

[6] C.-C. Lim, J. Yin, P.-I. Mak, H. Ramiah, and R. P. Martins, "An inverse-class-F CMOS VCO with intrinsic-high-Q 1st- and 2nd-harmonic resonances for $1/f^2$-to-$1/f^3$ phase-noise suppression achieving 196.2 dBc/Hz FOM," in *IEEE Int. Solid-State Circuits Conf. (ISSCC) Dig. Tech. Papers*, Feb. 2018, pp. 374–376, doi: 10.1109/ISSCC.2018.8310340.

[7] H. Guo, Y. Chen, P.-I. Mak, and R. P. Martins, "A 0.08 mm^2 25.5-to-29.9 GHz multi-resonant-RLCM-tank VCO using a single-turn multi-tap inductor and CM-only capacitors achieving 191.6 dBc/Hz FoM and 130 kHz $1/f^3$ PN corner," in *IEEE Int. Solid-State Circuits Conf. (ISSCC) Dig. Tech. Papers*. Piscataway, NJ, USA: Institute of Electrical and Electronics Engineers, Feb. 2019, pp. 410–412, doi: 10.1109/ISSCC.2019.8662470.

[8] S. S. Broussev, I. S. Uzunov, and N. T. Tchamov, "Design considerations in tapped-inductor fourth-order dual-band VCO," *IEEE Trans. Circuits Syst. II, Exp. Briefs*, vol. 59, no. 1, pp. 6–10, Jan. 2012, doi: 10.1109/TCSII.2011.2177697.

[9] N. T. Tchamov, S. S. Broussev, I. S. Uzunov, and K. K. Rantala, "Dual-band LC VCO architecture with a fourth-order resonator," *IEEE Trans. Circuits Syst. II, Exp. Briefs*, vol. 54, no. 3, pp. 277–281, Mar. 2007, doi: 10.1109/TCSII.2006.888732.

[10] S. V. Krishnaswamy, J. D. Adam, and M. Aumer, "P1J-4 high-Q FBARs using epitaxial AlN films," in *Proc. IEEE Ultrason. Symp.*, vol. 1, Oct. 2006, pp. 1467–1470, doi: 10.1109/ULTSYM.2006.369.

[11] H.-Y. Tsai and R.-B. Wu, "Tunable filter by FBAR using coupling capacitors," in *Proc. Asia–Pacific Microw. Conf. (APMC)*. Piscataway, NJ, USA: Institute of Electrical and Electronics Engineers, Nov. 2018, pp. 609–611, doi: 10.23919/APMC.2018.8671679.

[12] M. M. Torunbalci, T. J. Odelberg, S. Sridaran, R. C. Ruby, and S. A. Bhave, "An FBAR circulator," *IEEE Microw. Wireless Compon. Lett.*, vol. 28, no. 5, pp. 395–397, May 2018, doi: 10.1109/LMWC.2018.2815271.

[13] Z. Zhang, M. Zhi, Q. Ju, L. Tang, and D. Qiao, "Simulation of high-Q thin film bulk acoustic wave resonator for chip-scale atomic clock," in *Proc. IEEE Int. Nanoelectron. Conf. (INEC)*. Washington, DC, USA: IEEE Computer Society, May 2016, pp. 1–2, doi: 10.1109/INEC.2016.7589256.

[14] E. K. Lee, C. S. Kim, J. J. Kim, and H. R. Choi, "A study on the fabrication and evaluation of the MEMS based FBAR filter for wireless systems," in *Proc. 20th Int. Conf. Adv. Commun. Technol. (ICACT)*. Piscataway, NJ, USA: Institute of Electrical and Electronics Engineers, Feb. 2018, pp. 21–24, doi: 10.23919/ICACT.2018.8323632.

[15] A. Bhadauria, B. Panchal, and S. Varghese, "RF bandpass filters using FBAR with fractal electrodes," in *IEEE MTT-S Int. Microw. Symp. Dig.*, Nov. 2018, pp. 1–3, doi: 10.1109/IMaRC.2018.8877300.

[16] S. Lee and A. Mortazawi, "BAW filter design method based on intrinsically switchable ferroelectric BST FBARs," in *IEEE MTT-S Int. Microw. Symp. Dig.* Piscataway, NJ, USA: Institute of Electrical and Electronics Engineers, May 2016, pp. 1–4, doi: 10.1109/MWSYM.2016.7540105.

[17] A. C. Fischer *et al.*, "Integrating MEMS and ICs," *Microsyst. Nanoeng.*, vol. 1, p. 15005, May 2015, doi: 10.1038/micronano.2015.5.

[18] B. Bahr, Y. He, Z. Krivokapic, S. Banna, and D. Weinstein, "32 GHz resonant-fin transistors in 14 nm FinFET technology," in *IEEE Int. Solid-State Circuits Conf. (ISSCC) Dig. Tech. Papers*, Feb. 2018, pp. 348–350, doi: 10.1109/ISSCC.2018.8310327.

[19] A. Khelif and A. Adibi, *Phononic Crystals: Fundamentals and Applications*. New York, NY, USA: Springer-Verlag, 2015.

[20] R. Hudeczek and P. Baumgartner, "Polarization independent band gaps in CMOS back-end-of-line for monolithic high-Q MEMS resonator confinement," *IEEE Trans. Electron Devices*, vol. 67, no. 11, pp. 4578–4581, Nov. 2020, doi: 10.1109/TED.2020.3025521.

[21] F. H. Featherston and J. R. Neighbours, "Elastic constants of tantalum, tungsten, and molybdenum," *Phys. Rev.*, vol. 130, no. 4, pp. 1324–1333, May 1963, doi: 10.1103/PhysRev.130.1324.

[22] J. Zizka, S. King, A. G. Every, and R. Sooryakumar, "Mechanical properties of low- and high-k dielectric thin films: A surface Brillouin light scattering study," *J. Appl. Phys.*, vol. 119, no. 14, Apr. 2016, Art. no. 144102, doi: 10.1063/1.4945672.

[23] J. J. Wortman and R. A. Evans, "Young's modulus, shear modulus, and Poisson's ratio in silicon and germanium," *J. Appl. Phys.*, vol. 36, no. 1, pp. 153–156, Jan. 1965, doi: 10.1063/1.1713863.

[24] G. Carlotti, L. Doucet, and M. Dupeux, "Elastic properties of silicon dioxide films deposited by chemical vapour deposition from tetraethylorthosilicate," *Thin Solid Films*, vol. 296, nos. 1–2, pp. 102–105, Mar. 1997, doi: 10.1016/S0040-6090(96)09346-7.

[25] A. K. Chopra, *Numerical Evaluation of Dynamic Response*. Upper Saddle River, NJ, USA: Prentice-Hall, 2012.

[26] U. Fano, "Effects of configuration interaction on intensities and phase shifts," *Phys. Rev.*, vol. 124, no. 6, pp. 1866–1878, 1961, doi: 10.1103/PhysRev.124.1866.

[27] A. M. Martínez-Argüello, M. Martínez-Mares, M. Cobián-Suárez, G. Báez, and R. A. Méndez-Sánchez, "A new fano resonance in measurement processes," *Europhys. Lett.*, vol. 110, no. 5, p. 54003, Jun. 2015, doi: 10.1209/0295-5075/110/54003.

[28] K. M. Lakin, "Equivalent circuit modeling of stacked crystal filters," in *Proc. 35th Annu. Freq. Control Symp.*, May 1981, pp. 257–262, doi: 10.1109/FREQ.1981.200482.

[29] V. Choudhary and K. Iniewski, *MEMS: Fundamental Technology and Applications* (Devices, Circuits, and Systems). New York, NY, USA: Taylor & Francis, 2013.

[30] Y. Yang, R. Lu, T. Manzaneque, and S. Gong, "Toward Ka band acoustics: Lithium niobate asymmetrical mode piezoelectric MEMS resonators," in *Proc. IEEE Int. Freq. Control Symp.*, May 2018, pp. 1–5, doi: 10.1109/FCS.2018.8597475.

[31] J. L. Ma, Z. F. Fu, Q. Wei, and H. M. Zhang, "Uniaxial stress induced electron mobility enhancement in silicon," *Silicon*, vol. 5, no. 3, pp. 219–224, Jul. 2013, doi: 10.1007/s12633-013-9144-4.

[32] D. Yu, Y. Zhang, and F. Liu, "First-principles study of electronic properties of biaxially strained silicon: Effects on charge carrier mobility," *Phys. Rev. B, Condens. Matter Mater. Phys.*, vol. 78, no. 24, pp. 1–8, Dec. 2008, doi: 10.1103/PhysRevB.78.245204.

[33] *IRE Standards on Piezoelectric Crystals—The Piezoelectric Vibrator: Definitions and Methods of Measurement*, Standard 3, Institute of Radio Engineers, 1957.

[34] J. D. Larson, III, P. D. Bradley, S. Wartenberg, and R. C. Ruby, "Modified Butterworth–van Dyke circuit for FBAR resonators and automated measurement system," in *Proc. IEEE Ultrason. Symp.*, vol. 1, Oct. 2000, pp. 863–868, doi: 10.1109/ULTSYM.2000.922679.

[35] F. Javid, H. Aboushady, N. Beilleau, and D. Morche, "The design of RF bandpass $\Sigma\Delta$ modulator with bulk acoustic wave resonators," in *Proc. IEEE Int. Symp. Circuits Syst.*, May 2009, pp. 3138–3141, doi: 10.1109/ISCAS.2009.5118468.

[36] S. Khandelwal *et al. BSIM-CMG 110.0.0, Multi-Gate MOSFET Compact Model, Technical Manual*. Accessed: Apr. 20, 2020. [Online]. Available: http://bsim.berkeley.edu/models/bsimcmg/

[37] D. Lu *et al.*, *FinFET Modeling for IC Simulation and Design: Using the BSIM-CMG Standard*. New York, NY, USA: Academic, Mar. 2015.

[38] S. Dhar, E. Ungersböck, H. Kosina, T. Grasser, and S. Selberherr, "Electron mobility model for ⟨110⟩ stressed silicon including strain-dependent mass," *IEEE Trans. Nanotechnol.*, vol. 6, no. 1, pp. 97–100, Jan. 2007, doi: 10.1109/TNANO.2006.888533.